

# Calculation of electric fields induced by body and head motion in high-field MRI

Feng Liu,<sup>b</sup> Huawei Zhao,<sup>a</sup> and Stuart Crozier<sup>b,\*</sup>

<sup>a</sup> *The Centre for Magnetic Resonance, The University of Queensland, St. Lucia, Brisbane, Qld 4072, Australia*

<sup>b</sup> *The School of Information Technology and Electrical Engineering, The University of Queensland, Center for Magnetic Resonance, Research Road St. Lucia, Brisbane, Qld 4072, Australia*

Received 7 August 2002; revised 19 November 2002

## Abstract

In modern magnetic resonance imaging (MRI), patients are exposed to strong, nonuniform static magnetic fields outside the central imaging region, in which the movement of the body may be able to induce electric currents in tissues which could be possibly harmful. This paper presents theoretical investigations into the spatial distribution of induced electric fields and currents in the patient when moving into the MRI scanner and also for head motion at various positions in the magnet. The numerical calculations are based on an efficient, quasi-static, finite-difference scheme and an anatomically realistic, full-body, male model. 3D field profiles from an actively shielded 4 T magnet system are used and the body model projected through the field profile with a range of velocities. The simulation shows that it possible to induce electric fields/currents near the level of physiological significance under some circumstances and provides insight into the spatial characteristics of the induced fields. The results are extrapolated to very high field strengths and tabulated data shows the expected induced currents and fields with both movement velocity and field strength.

© 2003 Elsevier Science (USA). All rights reserved.

*Keywords:* MRI; High magnetic field; Induced current; Human body model

## 1. Introduction

Technological advances in magnetic resonance imaging (MRI) (higher static fields, faster gradients, stronger RF transmitters) have appeared rapidly and thus the potential for unwanted side effects of MRI increases. Many questions regarding the safety of these developments remain unanswered [1–6]. For example, to enhance the signal to noise ratio (SNR) and chemical shift dispersion (CSD), the static magnetic field strength has been increased and many high field MRI systems above 3T are in use. Understanding the interactions between the electromagnetic fields generated by MRI systems and the human body has become more significant with the push to high field strengths. The safety considerations for patients exposed to pulsed gradient and RF fields in MRI have, and continue to be, investigated extensively.

The static magnetic fields used in MRI may be associated, in varying degrees, with biological influences such as diamagnetic and paramagnetic effects [5,6]. Another concern in high-field MRI is related not to the strength of the static magnetic field, but to electromagnetic induction. The 3D pattern of the static magnetic field can induce current in moving conductive objects. This study is motivated by the anecdotal evidence that some patients experience uncomfortable sensations when moved into MRI or when moving their head during entry to the scanner or once in the system. Reported sensations include a feeling of falling, magnetophosphenes (light flashes), a loss of proprioception, a metallic taste in the mouth or muscle twitching (peripheral nerve stimulation).

This paper provides a numerical solution for the calculation of the spatial distributions of the induced currents and fields for magnetic stimulation by movement through static field distributions. In the literature, there are a variety of numerical approaches, including finite-difference time/frequency-domain (FDTD/FDFD), finite

\* Corresponding author. Fax: +61-7-3365-4999.

E-mail address: [stuart@itee.uq.edu.au](mailto:stuart@itee.uq.edu.au) (S. Crozier).

element (FE) or method of moment (MOM) techniques have been developed to calculate the fields induced in anatomic models of the human body [5]. Although the FE method is adaptable to irregular objects and together with the FDTD method provides the full-wave solutions, they usually require long computation times, especially when studying millimetre-resolution human models. In this work, we have used an efficient quasi-static finite difference formulation and a realistic model of an adult male with segmented tissue types. It is hoped that this study will help in the evaluation of the risks involved with patient movement in intense static fields.

## 2. Methods

### 2.1. Computational method

In order to calculate the induced fields during patient movement we first review the proposed computational method. According to Faraday's law, electric field  $\mathbf{E}$  in a sample can be generated by time-varying magnetic fields. Introducing the potential functions, the induced electric field can be expressed by

$$\mathbf{E} = -\frac{\partial \mathbf{A}}{\partial t} - \nabla \Phi, \quad (1)$$

where  $\mathbf{A}$  and  $\Phi$  are the vector magnetic potential and scalar electric potential, respectively.

In conductive samples, changes in the magnetic field  $\mathbf{B} = \nabla \times \mathbf{A}$  cause a flow of current  $\mathbf{J}_1 = \sigma(-\partial \mathbf{A}/\partial t)$ ,  $\sigma$  being the sample's conductivity. Any conductivity differences along the path of the current cause nonuniformity of accumulating electric charges, giving rise to scalar potential  $\Phi$ , the negative gradient of which causes a flow of current  $\mathbf{J}_2 = \sigma(-\nabla \Phi)$ .

In nonmagnetic material space, conservation of current density  $\mathbf{J} = \mathbf{J}_1 + \mathbf{J}_2$  dictates that

$$\nabla \cdot \mathbf{J} = \nabla \cdot (\sigma \mathbf{E}) = 0. \quad (2)$$

In this continuity equation, the charge term  $\partial \rho/\partial t$  is ignored by assuming that the subject motion is slow enough for this term to be insignificant.

According to the divergence theorem, Eq. (2) can be solved in integral form and then converted from a volume integral into a closed surface integral, resulting in

$$\int_S (\sigma \nabla \Phi) \cdot d\mathbf{S} = \int_S \left( \sigma \frac{\partial \mathbf{A}}{\partial t} \right) \cdot d\mathbf{S}. \quad (3)$$

This is the governing equation subject to the boundary condition that the component of the current density (and, therefore, the E-field) normal to the surface of the conductive object is zero.

This relationship can be solved for the scalar potential using a finite difference approximation method. We divide the computational space into a large number of cubic cells and then Eq. (3) is approximated for each

elementary cell. After discretization and rearrangement, the scalar potential for cell  $(i, j, k)$  can be expressed as

$$\Phi_{i,j,k} = \frac{\sum_{m=0}^1 \left( \Phi_{i+m,j,k} \sigma_{i+m,j,k}^a + \Phi_{i,j+m,k} \sigma_{i,j+m,k}^a + \Phi_{i,j,k+m} \sigma_{i,j,k+m}^a \right) - f(\mathbf{A})h}{\sum_{m=0}^1 \left( \sigma_{i+m,j,k}^a + \sigma_{i,j+m,k}^a + \sigma_{i,j,k+m}^a \right)}, \quad (4)$$

where  $f(\mathbf{A})$  is defined as

$$f(\mathbf{A}) = \sum_{m=0}^1 \left( \begin{array}{l} \left( \sigma_{i+m,j,k}^a \frac{\partial \mathbf{A}}{\partial t} (i+m,j,k) \right) \cdot \hat{\mathbf{s}}_x^m + \\ \left( \sigma_{i,j+m,k}^a \frac{\partial \mathbf{A}}{\partial t} (i,j+m,k) \right) \cdot \hat{\mathbf{s}}_y^m + \\ \left( \sigma_{i,j,k+m}^a \frac{\partial \mathbf{A}}{\partial t} (i,j,k+m) \right) \cdot \hat{\mathbf{s}}_z^m \end{array} \right), \quad (5)$$

in which  $i, j, k$  indicate the cell index,  $m$  indicates two faces (represented by "0, 1") in  $x, y, z$  directions, respectively,  $\hat{\mathbf{s}}$  is the unit vector normal to the cell faces and  $h$  is the cell size,  $\sigma^a$  is the local harmonic averaged conductivity.

Eq. (4) can be solved directly using an iterative algorithm that we have recently developed [7]. After the scalar potential has been calculated, the electric field components can be found using Eq. (1). The method was verified against analytic solutions for a low frequency problem, full details are given in [7], which indicated that the quasi-static assumption is reasonable for the analysis of lossy dielectrics in these circumstances.

### 2.2. The human model

The human model used in this work was obtained from the United States Air Force Research Laboratory (<http://www.brooks.af.mil/AFRL/HED/hedr/>), which represents a large male (see Fig. 1). The original spatial resolution of the model is 2 mm and the height of the model is 1.87 m. For the computations presented here, the model is mapped onto a 6-mm grid with volume-averaged dielectric and conductive properties. These properties change with frequency.

### 2.3. Static magnetic field

For the whole-body MRI systems, magnetic field strengths can perhaps be divided into high field (1.0–3.0 T), very high field (3.0–7.0 T) and ultra high field ( $\geq 7$  T). For this work, 4.0 T static magnetic fields are generated by a compact, symmetric, actively shielded MRI magnet [8,9]. For this magnet, the total coil length is 1.5 m with a homogeneous imaging region (DSV) of diameter is 50 cm, the shielding area (to 0.5 mT) is 4.5 m in the  $Z$ -direction and 4.0 m in the radial direction from the magnet iso-center.

The magnetic field pattern of the magnet is contoured for the  $y = 0$  coronal plane in Fig. 1(a). In this figure, the contours are of constant values of the  $z$ -component

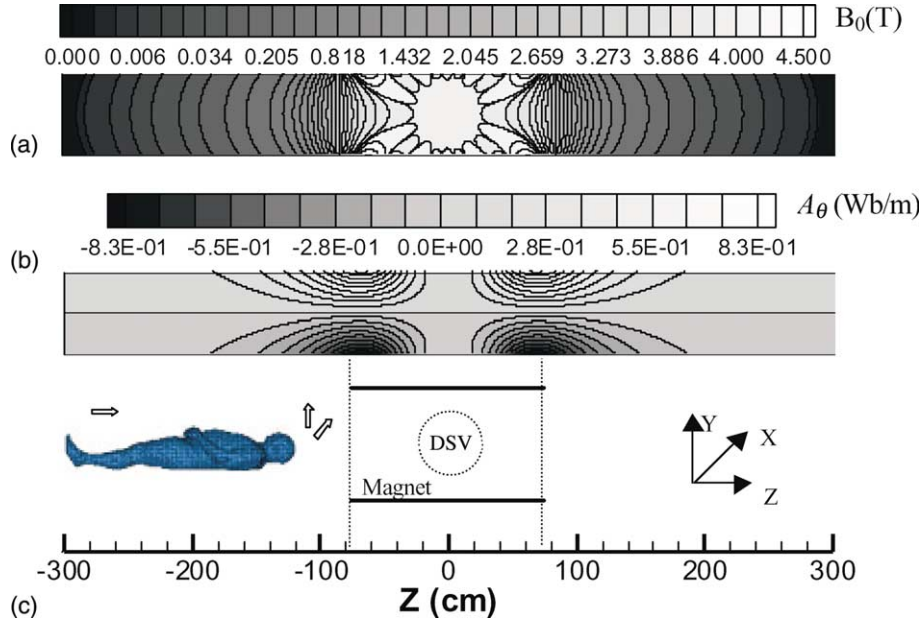


Fig. 1. The model of the human body moving into the cylindrical MRI Scanner: (a) the profile of the main static fields  $B_0$  (Tesla,  $z$ -component) in the  $y = 0$  plane; (b) the profile of the vector magnetic potential  $A_\theta$  (Wb/m) in the  $y = 0$  plane (in this plane, the radial component  $A_r = 0$ ); (c) the human body model moving into the main magnet.

of magnetic field,  $B_z$ . By examining the contours it is straightforward to see a bunching of the contours at the ends of the magnet (see also Fig. 1(c)). This is where the gradients of the static field are the largest. Specifically, within the zone occupied by human body, the maximum numerical value of  $\partial B_z / \partial z$  and  $B_z \partial B_z / \partial z$  are 12.9 T/m (at  $(r, z) = (0.33 \text{ m}, 0.79 \text{ m})$ ) and  $45.8 \text{ T}^2/\text{m}$  (at  $(r, z) = (0.33 \text{ m}, 0.75 \text{ m})$ ), respectively. On the  $z$ -axis, the peak  $\partial B_z / \partial z$ ,  $B_z \partial B_z / \partial z$  are 6.4 T/m (at  $(r, z) = (0 \text{ m}, 0.87 \text{ m})$ ) and  $17.7 \text{ T}^2/\text{m}$  (at  $(r, z) = (0 \text{ m}, 0.78 \text{ m})$ ), respectively. The strong inhomogeneity of the fields in these regions means that they are likely places for inducing fields in the body.

### 3. Results and discussion

#### 3.1. Simulation results

In this simulation, the human body is studied at a cell size of 6 mm and so the entire computational domain is divided into a  $x \times y \times z = 98 \times 57 \times 313 \approx 1.75 \times 10^6$  voxel region and the body model is embedded in this bounding box. During the period when the human model is moving into the magnet, we register the transient induced currents and electric fields at each position in the body with respect to the DSV centre. Then the peak values and their positions in the human body are obtained for further evaluation.

We have calculated three Cartesian components  $A_x, A_y, A_z$  for each of the locations within the human body model. The calculated variations of the vector

magnetic potential components are sketched in Fig. 1(b). For the magnet coils, the currents are in circumferential direction with no  $Z$ -direction components, so  $A_z = 0$  for each cell. After the vector potential is obtained, the scalar potential can be calculated using an iterative, successive over relaxation (SOR) algorithm [7]. The simulation converged in an average of about 2500 iterations. The typical computation time is a few minutes on a SUN Enterprise 450 workstation.

We firstly consider movement of the body in the  $Z$ -direction into the scanner, consistent with a patient on an automated table. The second study examines the case of a patient moving his (the model is male) head in the  $X$ - or  $Y$ -direction.

#### 3.2. Patient moving into the scanner

For the simulation of the whole body moving into the magnet, a range of distances between the bed end and DSV centre of  $z = -3.0$ – $3.0 \text{ m}$  is considered and a velocity  $v_z$  of  $0.5 \text{ m/s}$  is first tested.

The induced potentials are calculated at each transient position of the patient bed relative to the magnet center. The time-varying magnetic flux in Eq. (5) is expressed by the difference of vector potentials  $d\mathbf{A}$  of two neighbouring cells divided by the time difference  $dt = h/v_z$ . So the source is defined as

$$f(\mathbf{A}) = \sum_{m=0}^1 \left( \begin{array}{l} \left( \sigma_{i+m,j,k}^a \frac{\mathbf{A}^{(i+m,j,k+1)} - \mathbf{A}^{(i+m,j,k)}}{h/v_z} \right) \cdot \hat{\mathbf{S}}_x^m + \\ \left( \sigma_{i,j+m,k}^a \frac{\mathbf{A}^{(i,j+m,k+1)} - \mathbf{A}^{(i,j+m,k)}}{h/v_z} \right) \cdot \hat{\mathbf{S}}_y^m + \\ \left( \sigma_{i,j,k+m}^a \frac{\mathbf{A}^{(i,j,k+m+1)} - \mathbf{A}^{(i,j,k+m)}}{h/v_z} \right) \cdot \hat{\mathbf{S}}_z^m \end{array} \right). \quad (6)$$

The spatial precision of the displacement is restricted to the cell-size and only translation in the Z-direction is considered in this example.

The induced electric fields and currents in each cell of the human body model were calculated; selected planes are illustrated in Figs. 2–4. The simulations indicate that these induced quantities have complicated distributions

due to the spatial 3D magnetic field patterns and the electrical heterogeneity of the body. It also shows that induced values of the electric fields can be larger than perhaps expected.

In Figs. 2–4, the distribution of the EMFs in three different sections, X–Z, X–Y and Y–Z in the human model are depicted for three transient positions:

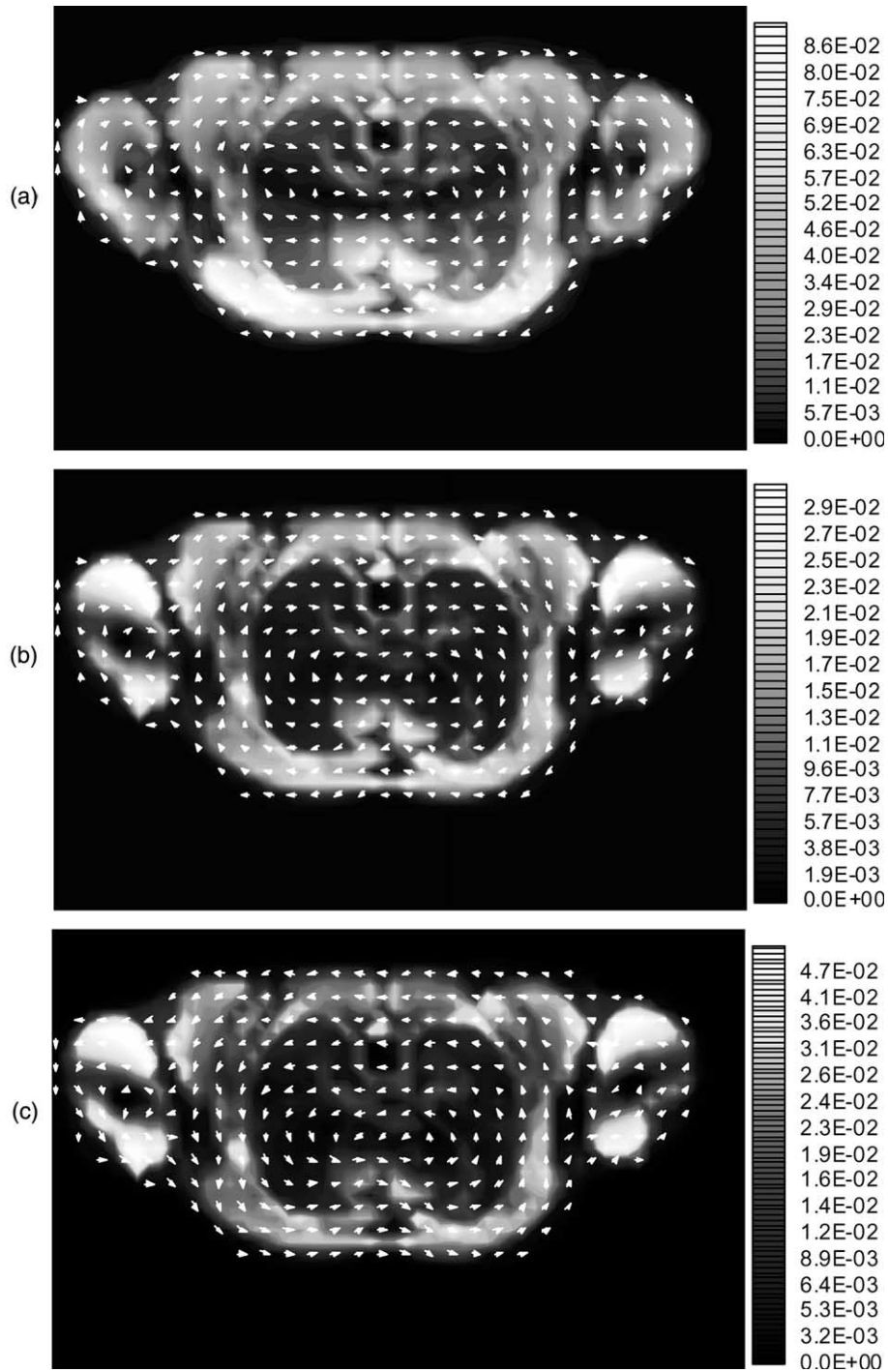


Fig. 2. The distribution of the current densities in a transverse section at the level of chest for three positions: (a)  $-2\text{ m}$ ; (b)  $-1.55\text{ m}$ ; and (c)  $-0.8\text{ m}$  with respect to the  $4\text{ T}$  magnet center. The patient velocity was  $0.5\text{ m/s}$ . The greyscale shows the magnitude of the induced current densities, and the arrows show the current direction. The unit is  $\text{A/m}^2$ .

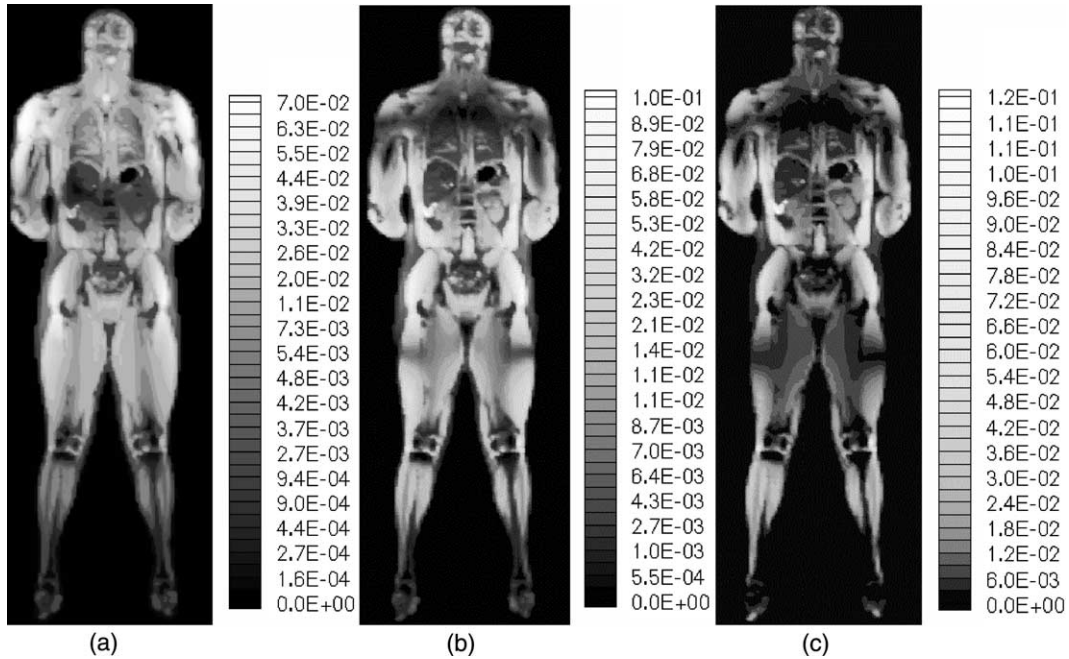


Fig. 3. The distribution of the current densities in a cross-section at  $y = 0.05$  m for three positions: (a)  $-2$  m; (b)  $-1.55$  m; and (c)  $-0.8$  m with respect to the DSV. The greyscale shows the magnitude of the induced current densities ( $A/m^2$ ).

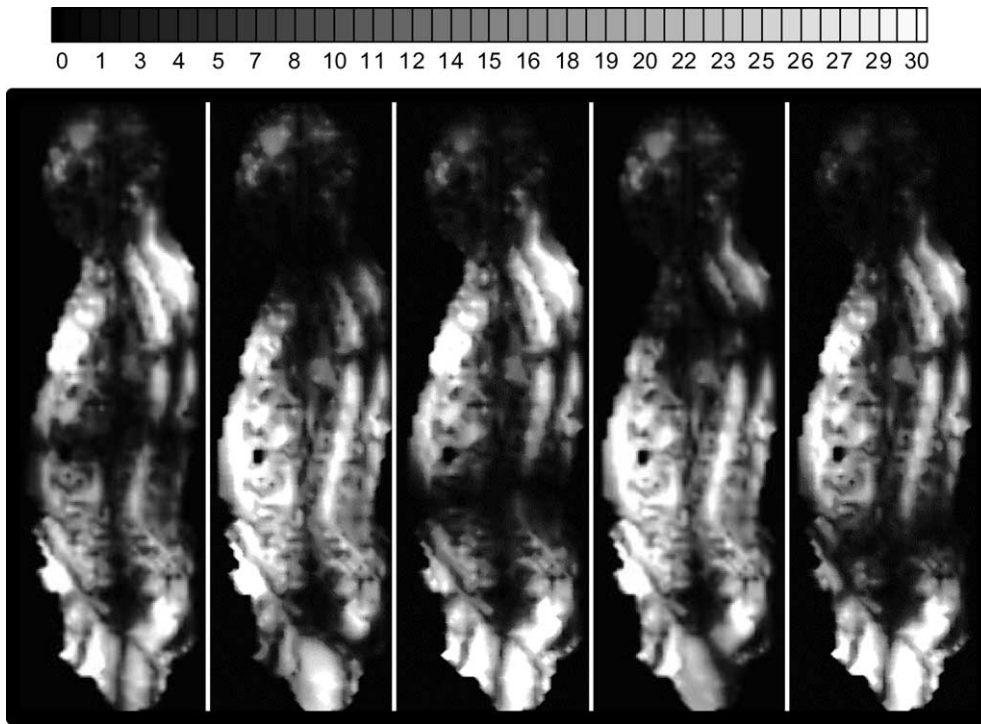


Fig. 4. The distribution of the electric gradient amplitude ( $V/m^2$ ) in a cross-section at  $x = 0.0$  m for five positions: (left–right:  $-2$  m,  $-1.6$  m,  $-1.2$  m,  $-0.8$  m, and  $-0.4$  m) with respect to the DSV. In this figures, a thresholding method (see legend) has been used for improved delineation.

(a)  $-2$  m; (b)  $-1.55$  m; and (c)  $-0.8$  m with respect to the DSV.

In Figs. 2 and 3, the greyscale shows the magnitude of the induced current densities ( $A/m^2$ ), and the arrows show the local current direction. For each position, the

field patterns are generally symmetrical in the  $X$ -direction due to the symmetry of the anatomy and electromagnetic source (see Figs. 1(a) and (b)). But in Figs. 2–4, some asymmetry of the patterns of induced EMFs can also be seen and are principally due to asymmetries of

the human body anatomy and corresponding differences in the local conductivity. Fig. 2 shows that the directions of the induced currents changes markedly during patient translation. The currents flow in different loops in different positions, and no normal currents flow at the body surface. The electromagnetic induction was stronger at positions near the end of the magnet than at other places, presumably due to the presence of stronger magnetic field gradients. This observation can be understood in simple terms as follows. Consider a circular loop of radius  $a$ , area  $A$ , centered on the  $z$ -axis with its plane perpendicular to this axis. The magnetic flux is  $\Phi = BA$  where  $B$  is the average value of  $B_z$  over the loop. The loop moves toward the magnet with velocity  $v$ . The induced EMF is  $d\Phi/dt$  and the induced E-field tangential to the loop is

$$\frac{1}{2\pi a} \frac{d\Phi}{dt} = \frac{\pi a^2}{2\pi a} \frac{dB}{dt} = \frac{a}{2} \frac{dB}{dz} \frac{dz}{dt} = \frac{a}{2} v \frac{dB}{dz}.$$

Therefore, the induced E-field is maximal at the end of the magnet where  $dB/dz$  is largest and zero at the magnet center where  $dB/dz$  is zero.

In nerve stimulation research, it has been shown that a peripheral nerve could be activated by the first derivative of the component of an induced E-field along a long, straight nerve fiber, during magnetic stimulation [10–12]. The locations with large values are usually the stimulation points. Although there is an open debate on this issue, the evaluation of the induced E-field gradients may be important in MRI related PNS. Therefore, E-field gradients are calculated in this study. Fig. 4 illustrates the induced E-field gradients pattern for the  $X = 0$  sagittal section. It shows that the induced E-field gradients changes markedly during the translation of the patient bed due to exposure to strong static magnetic gradients. The field values are depicted using a thresholding method. These regions occurred in areas such as the chest, back, lats, spine, hands, and groin. It is worth noting that in this figure, the amplitude of the E-field gradients are displayed. Detailed calculations of potential nerve stimulation should be based on both a full gradient tensor and nerve fibre directionality. The simulation shows that E-field gradients are higher in regions of the scapula, disk, arms, buttocks, and thigh. It is evident that large E-field gradients occur in regions where bones are close to the body surface and so these zones may be more excitable by a given applied field. Regions of high conductivity or large conductivity transitions also appear to be regions of high risk.

In this simulation, the positions of the peak current densities in the human model are registered and displayed in Fig. 5 (see black dots). These peak values occur in the chest, chest-arm interface, groin, and hands.

Fig. 6 provides curves describing the peak electric fields and current densities in the human model for all the positions along  $Z$ -axis with the patient moving into the

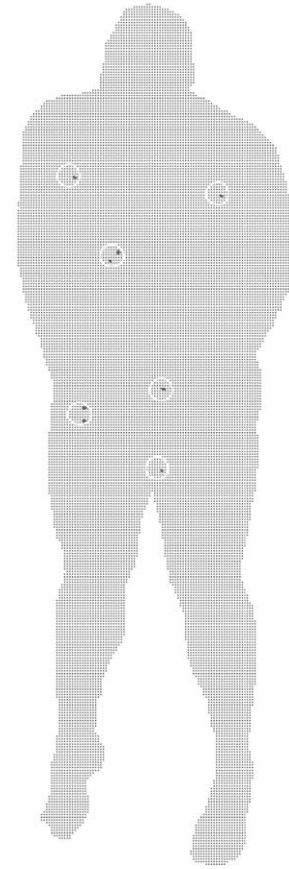


Fig. 5. Registered positions of the peak current densities in the human model for all the positions ( $z = -3.0$ – $0$ m) when the patient is moving into the 4 T magnet.

magnet at 0.5 m/s ((a) and (b)). In Fig. 6(a), the electric field and current density curves are both provided. These curves depict the obviously stronger electromagnetic induction when the body moves near a magnet-end, where the static magnetic field gradient is large. Fig. 6(b) shows the amplitudes of the two electric fields and current densities for maximum induction at various layers within the body. In this figure,  $|E|_1$  and  $|J|_1$  are the induced values when peak electric field (1.8 V/m) occurs, and  $|E|_2$  and  $|J|_2$  are the values when peak current density ( $0.21 \text{ A/m}^2$ ) happens. It can also be seen that the induced quantities are larger in the regions of the chest, abdomen/hands and thigh/groin, the peak values of the currents and electric field are not in the same positions. Based on the simulated data, a parameter  $J_p(v, B_0)$ , the peak current densities  $J$  vs. the velocity  $v$  and main magnetic field strength  $B_0$  can be estimated. After calculation,  $J_p(v, B_0) = J/v/B_0$  is about  $0.1 \text{ AS}/(\text{Tm}^3)$  for the bulk body movement. This value is based on the assumption that the peak currents are proportional to the magnetic field strength and velocity and are provided as extrapolated estimates only. Although the magnetic field profiles/patterns for different magnets are not the same as this 4 T system, this should provide some idea of the trend of the

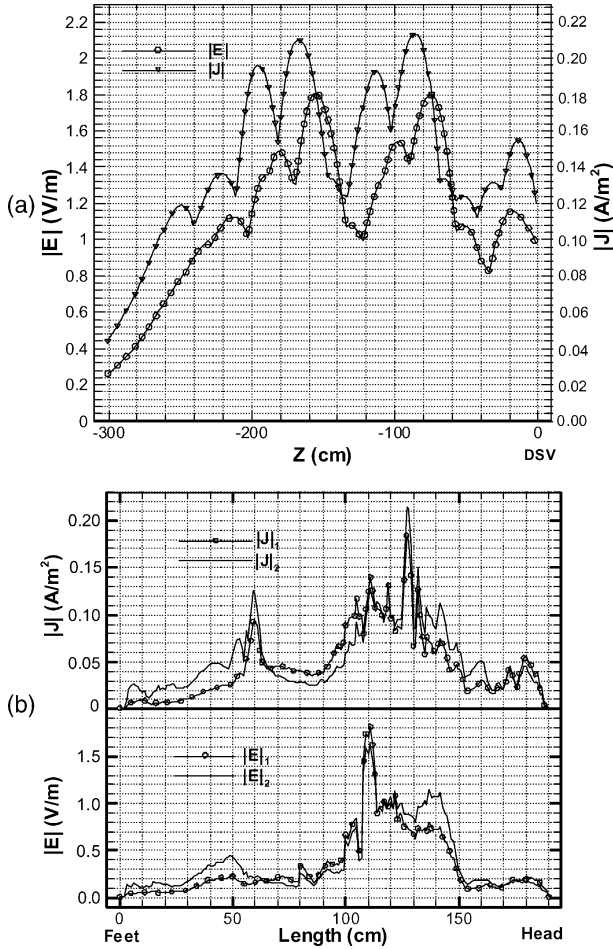


Fig. 6. Curves of the induced EMFs for the human body moving into the high-field MRI: (a) peak electric fields and current densities in the human model for all the positions ( $z = -3.0-0$  m) when the patient is moving into the 4 T magnet; (b) the amplitudes of the electric fields and current densities for the various layers of the human body model.  $|E|_1$  and  $|J|_1$  are the induced values when peak electric field (1.8 V/m) occurs;  $|E|_2$  and  $|J|_2$  are the values when peak current density (0.21 A/m<sup>2</sup>) occurs.

induced quantities. For example, for 8.0 T magnetic fields, if the patient velocity exceeds about 0.6 m/s, the induced fields/currents ( $J_p(v, B_0) = 0.1 \text{ AS/Tm}^3 \times 8 \text{ T} \times 0.6 \text{ m/S} = 0.48 \text{ A/m}^2$ ) approach the nerve stimulation thresholds/guidelines for low-frequency magnetic stimulation in MRI [4,13]. These effects correlate with a recent experiment [14]. In that study, entrance into an 8.0 T magnet and passage through the high gradient region elicited reactions from the subjects. They reported vertigo and metallic tastes in their mouths, as well as slight tingling effects. Most of these effects ceased once the subject was positioned at the isocenter.

### 3.3. Simulation of “head-shake”

Movement of the human head in transverse direction in the 4.0 T magnet was first simulated. For motion in Y-direction, Eq. (5) becomes

$$f(\mathbf{A}) = \sum_{m=0}^1 \left( \left( \sigma_{i+m,j,k}^a \frac{\mathbf{A}_{(i+m,j+1,k)} - \mathbf{A}_{(i+m,j,k)}}{h/v_y(k)} \right) \cdot \hat{S}_x^m + \left( \sigma_{i,j+m,k}^a \frac{\mathbf{A}_{(i,j+m+1,k)} - \mathbf{A}_{(i,j+m,k)}}{h/v_y(k)} \right) \cdot \hat{S}_y^m + \left( \sigma_{i,j,k+m}^a \frac{\mathbf{A}_{(i,j,k+m)} - \mathbf{A}_{(i,j,k+m-1)}}{h/v_y(k)} \right) \cdot \hat{S}_z^m \right). \quad (7)$$

In this equation,  $v_y$ , the velocity of the head, is determined by the layer number of the head ( $k$ ). In an attempt to simulate a realistic head movement, we assume that velocity of the top of the head is 0.2 m/s and decreases linearly to zero near the layers of the shoulder. The time-varying magnetic flux in Eq. (5) is expressed by the difference of vector potentials  $d\mathbf{A}$  of two neighbouring cells in Y-direction. Here the induced potentials are computed at positions  $z \in (-1.85-1.85)$  m, where the field gradients are larger.

Simulation of the movement in X-direction was made in a similar fashion.

The results are shown in Fig. 7. In Fig. 7(a), the electric field and current densities are given for  $z = 0-1.85$  m. Fig. 7(b) shows the amplitudes of the induced quantities for the various layers of the human head at the position  $z = 0.5$  m, where peak induced values occur. In this figure,  $|E|_x$  and  $|J|_x$  are the values for motion in X-direction, and  $|E|_y$  and  $|J|_y$  are the values for motion in the Y-direction. Based on the simulated data, the estimated peak current densities vs. the head velocity (X- and Y-) and main magnetic field strength  $B_0$   $J_p(v, B_0)$  is about 0.3 and 0.18 AS/(Tm<sup>3</sup>), respectively. These simulations show that in high field MRI systems, rapid head movement should be avoided. Furthermore, in the former mentioned experiment [14], vertigo was also reported when technicians moved their head rapidly within the bore of the 8.0 T magnet.

## 4. Discussion

Ever since the application of MRI, the interaction of the static magnetic fields with biological tissue has been questioned. As mentioned before, there are many aspects to the effects of the magnetic fields in biology. One mechanism of static magnetic field interaction with moving biological samples is via electromagnetic induction. Due to relatively low velocities involved in this case, the induced E-field component equal to  $-\partial\mathbf{A}/\partial t$  can be expressed without further calculation as  $\mathbf{v} \times \mathbf{B}_0$  [15]. It is the component equal to  $-\nabla\phi$  that is produced by the induced charge densities and that requires the complex calculation presented in this paper.

From the simulations, we can see that induced electric fields and currents of reasonable magnitude can be induced in patients moving in high-field MRI systems. To evaluate the potential of magnetic stimulation by body movement, a quantitative comparison can be made between these calculated induced quantities and results

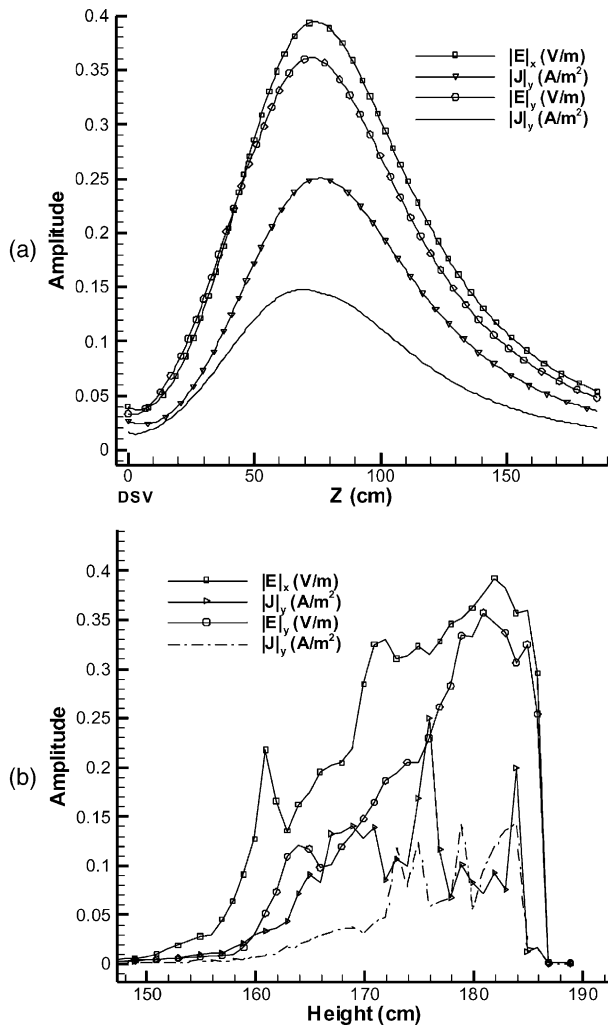


Fig. 7. The induced electric fields and currents for the human head movement in the high-field MRI. In all the figures, “x” is for the head moving in the left–right direction, and “y” for the up–down direction. (a) Peak electric fields and currents in the human model for all the positions of the head ( $z = 0$ – $1.85$  m) in the magnets; (b) the amplitudes of electric fields and currents for the various layers of the human model near the head.

obtained from the PNS studies of pulsed gradient fields in MRI. A review of magnetic stimulation by gradient coils can be found in [4]. Figs. 4 and 6 illustrate that the field magnitudes induced by body movement are less than those of gradient coils reported in the literature [4,16,17]. In this simulation, the maximum current is about  $220 \text{ mA/m}^2$ , while for the gradient coils in modern MRI scanners, Faraday currents can reach  $386 \text{ mA/m}^2$  [13], while current FDA limits for the induced currents are less than  $480 \text{ mA/m}^2$  [4,13]. For the electric field, the peak value is about  $1.8 \text{ V/m}$  for the  $4 \text{ T}$ ,  $0.5 \text{ m/s}$  movement case, which is much smaller than  $6.2 \text{ V/m}$ , which has been suggested to be the threshold for nerve stimulation at low frequencies [16]. While the simulated values are all within the range of safety limits, the magnitudes of the current densities and the electric fields are in the same order as

those induced by time-varying gradient fields in MRI and should not be ignored. This is particularly so for magnets at  $4 \text{ T}$  and above. Although the fields calculated in this paper are suggested as being near the level of physiological significance and possibly harmful, they are substantially lower than those associated with transcranial magnetic stimulation (TMS), which is being widely used for diagnostic purposes.

In addition to the types of motion considered in this paper, very similar types of fields and effects can be produced by blood flow even when the patient’s body is nominally at rest [1,18–23]. These fields differ somewhat from those produced by table motion. Fields produced by table motion are maximal near the magnet ends where the magnetic field changes rapidly. Blood flow velocity in the aorta is on the order of  $1 \text{ m/s}$  and the aortic arch is more or less perpendicular to  $\mathbf{B}_0$ . This flow-induced emf will be greatest at the center of the magnet where  $\mathbf{B}_0$  is largest. At the center of a  $4 \text{ T}$  magnet a flow-induced field of about  $4 \text{ V/m}$  is present within this region of the aorta. It is worth noting that the methods of this paper could be used to calculate the total body distribution of E-field resulting from aortic and other arterial blood flow within the magnet. The effect of these flow-induced electrical potentials could distort the electrocardiogram taken in high field magnets. In addition, the Lorentz forces on blood flow caused by the induced E-fields and currents were once considered as possible safety issues due to the magnetohydrodynamic retarding force associated with them. It was later shown that these forces are not significant at the field strengths used in MRI [1].

## 5. Conclusion

In this paper, a heterogeneous volume conductor model of an adult male along with an efficient finite difference scheme was used to calculate the induced electric field distributions when the human body moves into high field MRI scanners. The simulations show that the induced fields and currents should not be ignored at ultrahigh fields. Extrapolated data of the peak induced currents has been presented to evaluate the potential safety issue at a variety of field strengths and patient velocities. Surprisingly high values for the induced quantities may be generated for patients who move rapidly in the fields, particularly at the ends of the magnet systems. It is hoped that these results will better inform the MRI community concerning safe movements in or around an MRI system. The adage “slower is better,” is apt in this regard.

## Acknowledgments

Financial support for this project from the Australian Research Council is gratefully acknowledged.

## References

- [1] J.F. Schenck, Safety of strong, static magnetic fields, *J. Magn. Reson. Imag.* 12 (2000) 2–19.
- [2] J.F. Schenck, C.L. Dumoulin, R.W. Redington, H.Y. Kressel, R.T. Elliott, I.L. McDougall, Human exposure to 4.0-Tesla magnetic fields in a whole-body scanner, *Med. Phys.* 19 (1992) 1089–1098.
- [3] J.F. Schenck, Health and physiological effects of human exposure to whole-body four-tesla magnetic fields during MRI, in: R.L. Magin, R.P. Liburdy, B. Persson (Eds.), *Biological effects and safety aspects of nuclear magnetic resonance imaging and spectroscopy*, Annals of the New York Academy of Sciences, vol. 649, New York Academy of Sciences, New York, 1992, pp. 285–301.
- [4] F. Schmitt, M.K. Stehling, R. Turner, *Echo-Planar Imaging Theory, Technique and Application*, Springer, New York, 1998.
- [5] C. Polk, E. Postow, *Handbook of Biological Effects of Electromagnetic Fields*, CRC, New York, 1996.
- [6] A. Kangarlu, P.-M.L. Robitaille, Biological effects and health implications in magnetic resonance imaging, *Concepts Magn. Reson.* 12 (2000) 321–359.
- [7] F. Liu, S. Crozier, H. Zhao, On the induced electric field gradients in the human body for magnetic stimulation by gradient coils in MRI. *IEEE Trans. Biomed. Eng.* in press.
- [8] S. Crozier, C. Snape-Jenkinson, L.K. Forbes, The stochastic design of force-minimized compact magnets for high-field magnetic resonance imaging applications, *IEEE Trans. Appl. Supercon.* 11 (2001) 4014–4022.
- [9] H. Zhao, S. Crozier, D.M. Doddrell, Compact clinical MRI magnet design using a multi-layer current density approach, *Magn. Reson. Med.* 45 (2001) 331–340.
- [10] H. Nakayama, T. Kiyoshi, H. Wada, K. Yunokuchi, Y. Tamari, 3-D analysis of magnetic stimulation to human cranium, in: *The 12th International Conference on Biomagnetism*, Espoo, Finland, 2000.
- [11] P.J. Basser, R. Wijesinghe, B.J. Roth, The activating function for magnetic stimulation derived from a three-dimensional volume conductor model, *IEEE Trans. Biomed. Eng.* 39 (1992) 1207–1210.
- [12] R. Liu, S. Ueno, Calculating the activating function of nerve excitation in inhomogeneous volume conductor during magnetic stimulation using finite element method, *IEEE Trans. Magn.* 36 (2000) 1796–1799.
- [13] O.P. Gandhi, X.B. Chen, Specific absorption rates and induced current densities for an anatomy-based model of the human for exposure to time-varying magnetic fields of MRI, *Magn. Reson. Med.* 41 (1999) 816–823.
- [14] A. Kangarlu, R.E. Burgess, H. Zhu, T. Nakayama, R.L. Hamlin, A.M. Abduljalil, P.M.L. Robitaille, Cognitive, cardiac, and physiological safety studies in ultra high field magnetic resonance imaging, *Magn. Reson. Imag.* 17 (1999) 1407–1416.
- [15] P. Lorrain, D.P. Corson, F.L. Freeman, *Electromagnetic Field and Waves*, New York, 1988.
- [16] R. Bowtell, R.M. Bowley, Analytic calculations of the E-fields induced by time-varying magnetic fields generated by cylindrical gradient coils, *Magn. Reson. Med.* 44 (2000) 782–790.
- [17] F. Liu, S. Crozier, H. Zhao, Finite-difference time-domain based studies of MRI pulsed field gradient-induced eddy currents inside the human body, *Concepts Magn. Reson.* 15 (2002) 26–36.
- [18] T. Togawa, O. Okai, M. Ohima, Observation of blood flow e.m.f. in externally applied strong magnetic fields by surface electrodes, *Med. Biol. Eng.* 5 (1967) 169–170.
- [19] D.E. Beischer, J.C. Knepton, Influence of strong magnetic fields on the electrocardiogram of squirrel monkeys (*Saimiri sciureus*), *Aerosp. Med.* 35 (1964) 939–944.
- [20] T.S. Tenforde, C.T. Gaffey, B.R. Moyer, T.F. Budinger, Cardiovascular alterations in Macaca monkeys exposed to stationary magnetic fields: experimental observations and theoretical analysis, *Bioelectromagnetics* 4 (1983) 1–9.
- [21] A.T. Winfrey, The electrical thresholds of ventricular myocardium, *J. Cardiovasc. Physiol.* 1 (1990) 393–410.
- [22] T.F. Budinger, Magneto-hydrodynamic retarding effect on blood flow velocity at 4.7 tesla found to be insignificant, in: *Book of Abstracts*, Berkeley, CA: Society of Magn. Reson. Med., 1987, p. 183.
- [23] J.R. Keltner, M.S. Roos, P.R. Brakeman, T.F. Budinger, Magneto-hydrodynamics of blood flow, *Magn. Reson. Med.* 16 (1990) 139–149.